

# Robotic Immobilization of Motile Sperm for Clinical Intracytoplasmic Sperm Injection

Zhuoran Zhang , Changsheng Dai , James Huang , Xian Wang, Jun Liu , Changhai Ru, Huayan Pu , Shaorong Xie, Junyan Zhang, Sergey Moskvotsev, Clifford Librach, Keith Jarvi , and Yu Sun 

**Abstract—Objective:** In clinical intracytoplasmic sperm injection (ICSI), a motile sperm must be immobilized before insertion into an oocyte. This paper aims to develop a robotic system for automated tracking, orientation control, and immobilization of motile sperms for clinical ICSI applications. **Methods:** We adapt the probabilistic data association filter by adding sperm head orientation into state variables for robustly tracking the sperm head and estimating sperm tail positions under interfering conditions. The robotic system also utilizes a motorized rotational microscopy stage and a new visual servo control strategy that predicts and compensates for sperm movements to actively adjust sperm orientation for immobilizing a sperm swimming in any direction. **Results:** The system robustly tracked sperm head with a tracking success rate of 96.0% and estimated sperm tail position with an accuracy of 1.08  $\mu\text{m}$  under clinical conditions where the occlusion of the target sperm and interference from other sperms occur. **Experimental results from robotic immobilization of 400 sperms confirmed that the system achieved a consistent immobilization success rate of 94.5%, independent of sperm velocity or swimming direction. Conclusion:** Our adapted tracking algorithm effectively distinguishes the target sperm from interfering sperms. Predicting and compensating for sperm movements significantly reduce the positioning error during sperm orientation control. These features make the robotic system suitable for automated sperm immobilization. **Significance:** The robotic system eliminates stringent skill requirements in manual sperm

immobilization. It is capable of manipulating sperms swimming in an arbitrary direction with a high success rate.

**Index Terms—Automation at micro-nano scales, biological cell manipulation, medical robotics.**

## I. INTRODUCTION

MANIPULATION of motile cells has attracted interest from both the robotics and cell biology fields. Due to their motile nature, motile cells (e.g., bacteria and sperm) have been used to build bio-hybrid microrobots for assembly [1] and cargo transportation (drug delivery) [2]. In biology, a motile cell needs to be manipulated and immobilized for biological and biochemical analysis. The task discussed in this paper is the robotic immobilization of a motile sperm, in a fully automated manner. Sperm immobilization is an essential step in sperm analysis in biology and in clinical intracytoplasmic sperm injection (ICSI) [3] where a sperm is immobilized before aspirated into a glass micropipette for insertion into an oocyte for fertilization. The ICSI procedure presently accounts for over 70% of *in vitro* fertilization (IVF) treatments globally [4].

Several techniques have been developed for the manipulation of motile cells, using motorized micromanipulators [5], optical tweezers [6], optoelectronic tweezers [7], lithography-based patterning [8], [9], fluidic flow [10], magnetic field [11], [12], electrical field [13], and acoustic field [14]. However, most of these techniques were developed for cell trapping (i.e., to restrict cell motion within a certain area while the cells remain motile), and thus, are not applicable to the task of permanently immobilizing a motile sperm.

Sperm immobilization is conventionally performed by highly trained embryologists who manipulate a micromanipulator to tap (press) the sperm tail against a surface (e.g., the substrate of a glass slide or Petri dish) with a glass micropipette (Fig. 1). Due to the fast movement of a healthy sperm ( $\geq 25 \mu\text{m/s}$ ) [15] and the small size and low visibility of the sperm tail ( $\leq 1 \mu\text{m}$  in diameter) [16], manual operation has stringent skill requirements, and success rates vary significantly across operators, demanding the reduction of human involvement and automated robotic manipulation.

Robotic sperm immobilization with a glass micropipette was attempted [17]. Based on computer vision and motion control, automated sperm tail tracking and tapping for immobilization

Manuscript received February 6, 2018; revised May 15, 2018; accepted June 15, 2018. Date of publication June 19, 2018; date of current version January 18, 2019. This work was supported in part by the Natural Sciences and Engineering Research Council of Canada through a Discovery Grant and Tier I Canada Research Chair and in part by the University of Toronto via a Connaught Innovation Award and also supported in part by the National Natural Science Foundation of China under Grant 61774107, Grant 61625304, and Grant 91748116, and in part by the Science and Technology Commission of Shanghai under Grant 16441909400. (Zhuoran Zhang and Changsheng Dai contributed equally to this work.) (Corresponding author: Yu Sun.)

Z. Zhang, C. Dai, J. Huang, X. Wang, J. Liu, and Y. Sun are with the Advanced Micro and Nanosystems Laboratory, Department of Mechanical and Industrial Engineering, University of Toronto, Toronto, ON M5S 3G8, Canada. (e-mail: sun@mie.utoronto.ca).

C. Ru is with the Research Center of Robotics and Micro System and Collaborative Innovation Center of Suzhou NanoScience and Technology, Soochow University.

H. Pu and S. Xie are with the School of Mechatronic Engineering and Automation, Shanghai University.

J. Zhang, S. Moskvotsev, and C. Librach are with the CReATe Fertility Centre.

K. Jarvi is with the Mount Sinai Hospital.

Digital Object Identifier 10.1109/TBME.2018.2848972

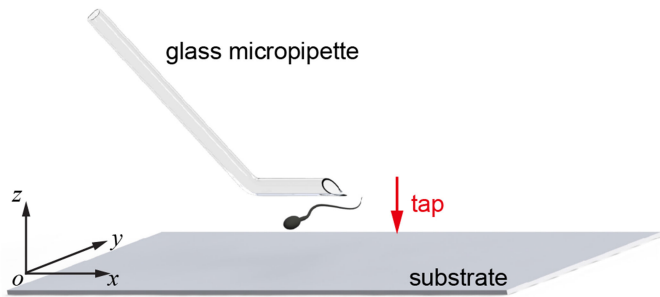


**Fig. 1.** Schematic illustration of motile sperm immobilization. A glass micropipette is controlled to tap (press) the sperm tail against the substrate for immobilization. Sperm DNA is all contained in the head; therefore, damage to sperm head must be avoided.

were achieved. However, two major limitations remain and must be tackled for robotic sperm immobilization to become clinically reliable. In [17], the success rate dropped significantly from 89.7% to 81.5% for immobilizing sperms with a high swimming velocity ( $>20 \mu\text{m/s}$ ); and only sperms swimming in the direction that is nearly perpendicular to the micropipette axis (Fig. 1) can be immobilized. However, sperms swim in all directions. Due to the lack of a rotational degree of freedom [17], micropipette tapping of sperms moving in other directions (e.g., parallel to the micropipette axis) would damage the sperm head where DNA is located.

To address the first challenge, visual feedback of both the sperm head and tail positions must be obtained throughout the immobilization process. In a clinical sample, the target sperm to track and immobilize is often interfered (e.g., crossover, occlusion) by other sperms. Although a number of algorithms have been developed for tracking motile cells [18]–[21], most of these algorithms are based on nearest neighbor tracking [22] and do not account for interference from other cells. Furthermore, existing algorithms for tracking the low-contrast sperm tail [23]–[25] become ineffective when occlusion occurs, which is caused by the micropipette tip during sperm tail tapping. To solve the second limitation, a rotational degree of freedom should be integrated into the micromanipulation system, such as via the integration of a motorized rotational microscopy stage [26], to actively adjust the orientation of the target sperm. Since the target sperm does not align with the rotational center of the rotational stage, rotation-induced translational displacements must be properly compensated for.

This paper presents a robotic system that is capable of immobilizing motile sperms with a consistent success rate of 94.5% ( $n = 400$  sperms), independent of sperm velocity and orientation. The system adapts the probabilistic data association filter for robustly tracking the sperm head and estimating the sperm tail position, robustly tackling interference from other sperms or contaminants. Using a motorized rotational microscopy stage and a new visual servo control strategy that predicts and compensates for sperm movements, the robotic system is capable of accurately controlling the orientation of a motile sperm and achieves reliable immobilization of sperms swimming in any direction.

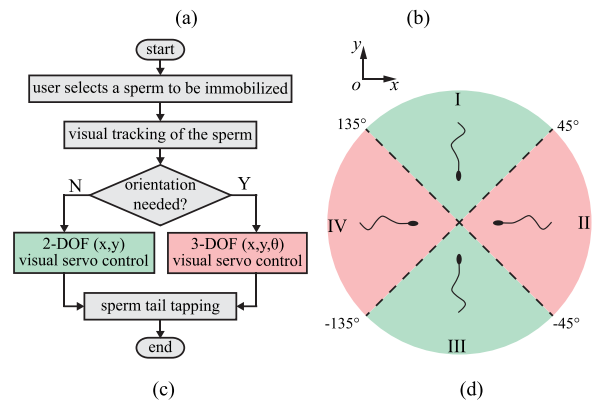
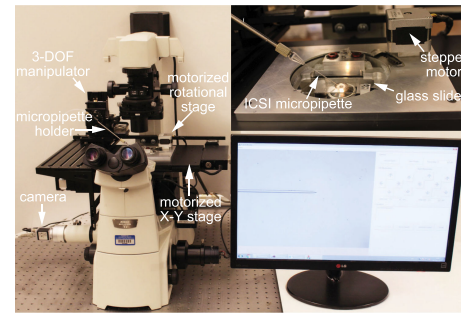


**Fig. 2.** (a) Robotic sperm immobilization system setup. (b) A motorized rotational stage is mounted on the X-Y translational stage to form a multi-DOF control system. (c) Overall operation sequence for robotic sperm immobilization. (d) Sperm are classified into four quadrants, based on their head orientations. The system performs both translational and rotational control via visual servoing to orient a target sperm in quadrants II and IV into quadrant I or III.

## II. SYSTEM OVERVIEW

### A. System Setup

As shown in Fig. 2(a), the system was built around a standard inverted microscope (Nikon Eclipse Ti-S) that is equipped with a motorized X-Y translational stage (ProScan, Prior Scientific Inc.). A motorized rotational stage (maximum angular velocity:  $720^\circ/\text{s}$ ) that we previously developed [26] is mounted on the X-Y translational stage to form a multi-DOF position control system [see Fig. 2(b)]. A camera (Basler acA1300-30gc, resolution:  $1200 \times 900$  pixels) is connected to the microscope to provide visual feedback. Sperms are visualized under the differential interference contrast (DIC) imaging mode for better imaging contrast. Images are captured at 30 frames per second with a  $20\times$  objective (Nikon S Plan Fluor, NA: 0.45). The rate of 30 frames per second is sufficiently fast for tracking sperm tails whose beating frequency is 5–10 Hz [16]. A standard clinical ICSI micropipette (Origio MIC-50-35, inner diameter:  $5.0 \mu\text{m}$ , tilted angle:  $35^\circ$ ) is mounted on a motorized 3-DOF translational micromanipulator (MP285, Sutter Inc.) with the micropipette tip parallel to the substrate of the glass slide for robotic sperm immobilization.

### B. Operation Sequence

For automated robotic micromanipulation, an end-effector auto-locating algorithm [27] automatically brings the

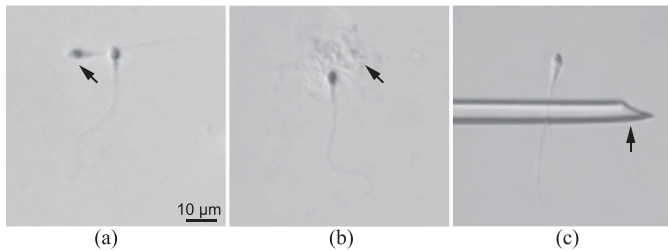


**Fig. 3.** Under clinical conditions, the head of a target sperm can be interfered by (a) other sperms or (b) contaminants (black arrows). (c) During sperm tail tapping, the sperm tail is unavoidably occluded by the micropipette, lowering its visibility even further.

micropipette into the field of view. Vision-based contact detection is then performed to determine the relative vertical distance between the micropipette tip and the substrate [28], after which the micropipette is placed at  $25 \mu\text{m}$  above the substrate. Note that the aforementioned steps only need to be performed once on the initiation of the system. In experiments, a human operator indicates a sperm of interest via computer mouse clicking [see Fig. 2(c)]. This permits exercising the human operator's expertise/know-how for sperm selection. The system then begins to visually track the sperm head and estimate the sperm tail position. Visual servo control is performed to move the sperm of interest to the center of the field of view as well as to adjust the orientation of the sperm. The micromanipulator is controlled to undergo a sequence of motions to tap the sperm tail against the substrate to immobilize the sperm. The immobilized sperm is ready to be aspirated into the micropipette and inserted into an oocyte. The micropipette is then controlled to move back to its original position, ready for immobilizing the next sperm.

The visual servo control step in Fig. 2(c) branches out into two scenarios, based on the orientation of the target sperm. The orientation refers to the angle between the major axis of the sperm head and the horizontal axis of the image frame. Sperms swimming in all directions are classified into four quadrants [Fig. 2(d)]. Ideally, the tail of the target sperm should be nearly perpendicular to the micropipette axis. Since the micropipette is fixed on the micromanipulator at  $0^\circ$  (Fig. 1), and the micromanipulator has only three translational degrees of freedom, sperm in quadrants I and III are ready for immobilization and only X-Y translation control of the motorized stage via visual servoing is required to keep the sperm within the field of view. For a sperm in quadrants II and IV, direct micropipette tapping of the sperm tail could undesirably damage the sperm head where DNA is located. Hence, 3-DOF visual servo control (X-Y translation and rotation) of the X-Y translational stage and the rotational stage is performed by the system to actively adjust the orientation of the sperm into quadrant I or III.

### III. SPERM VISUAL TRACKING

To immobilize a sperm, visual feedback of both sperm head and tail positions is required for visual servo control. In a clinical sample, the head of the target sperm (typical head length:  $4.1 \mu\text{m}$ , width:  $2.8 \mu\text{m}$ ) can be interfered by other sperms or contaminants [Fig. 3(a)(b)]. Additionally, during sperm tail tapping,

as shown in Fig. 3(c), the micropipette unavoidably occludes the sperm tail that is smaller than  $1 \mu\text{m}$  in diameter and already has very low visibility and contrast even without occlusion. To obtain visual feedback of both sperm head and tail positions, we developed algorithms 1) to robustly track the sperm head under interference, and 2) to estimate the position of the low-contrast sperm tail.

#### A. Sperm Head Tracking

Tracking is initialized by a human operator's computer mouse clicking to select a sperm of interest (i.e., the target sperm). Considering multiple sperms are detected/measured in each image frame, the tracking algorithm essentially associates candidate sperm positions to the target sperm. Under interference from other sperms, the detected candidate positions may not originate from the target sperm but from an interfering sperm [see Fig. 3(a)], yielding uncertainty in data association. Hence, we adapted the standard probabilistic data association filter (PDAF) [29] to deal with data association uncertainty for robust sperm tracking under interference. Briefly, PDAF follows a predict-update cycle, similar to the Kalman filter. Compared to the Kalman filter, the PDAF method additionally performs a validation process to select valid measurements, and an association probability is computed for each valid measurement. The association probability is then used as weight for state update.

Different from the standard PDAF method where the target to track is modeled with only position and velocity information, for sperm tracking, we add sperm head orientation  $\theta$  to the target model and use sperm shape information to reduce uncertainty in data association. State variable  $X_k$  of the sperm at time (frame)  $k$  is modeled as

$$X_k = [x, y, \theta, \dot{x}, \dot{y}, \dot{\theta}]^T \quad (1)$$

where  $(x, y)$  is the 2D position of the sperm head obtained by calculating the centroid of the sperm head contour segmented by adaptive thresholding, and  $\theta$  is the angle between the major axis of the sperm head and the horizontal axis of the image frame.

Sperm dynamics is modeled as

$$X_k = FX_{k-1} + w_{k-1} \quad (2)$$

$$Z_k = HX_k + v_k \quad (3)$$

where  $F$  is the state-transition matrix,  $w_{k-1}$  is the process noise, and  $H$  and  $v_k$  are the measurement matrix and measurement noise, respectively.  $F$  and  $H$  are given by

$$F = \begin{bmatrix} I_3 & I_3 T \\ 0_3 & I_3 \end{bmatrix}, \text{ and } H = [I_3 \quad 0_3],$$

where  $T$  is the time interval between two successive measurements (i.e., image frames), and  $I_3$  and  $0_3$  are  $3 \times 3$  identity and zero matrices, respectively.

Since a typical sperm wiggles around an average path and changes its swimming speed and direction, we modify the constant process noise covariance matrix, which is commonly used in the standard PDAF method, to be adaptive to sperm's wiggly motion. The new adaptive process noise covariance matrix,

$Q_k$  is

$$Q_k = c_1 Q_{k-1} + c_2 (\hat{X}_k - \hat{X}_{k-1})(\hat{X}_k - \hat{X}_{k-1})^T + c_3 Q_0 \quad (4)$$

where  $\hat{X}_k = F X_{k-1}$  is the predicted sperm state at time instance  $k$ ;  $c_1$ ,  $c_2$ , and  $c_3$  are coefficients, and  $c_1 + c_2 + c_3 = 1$ ;  $Q_0$  is the initial process noise covariance matrix.

PDAF calculates the Mahalanobis distance,  $d_k$  between the predicted measurement  $\hat{Z}_k = H \hat{X}_k$  and the actual measurements  $Z_k = [x, y, \theta]^T$  for measurement validation

$$d_k(Z_k) = \sqrt{(Z_k - \hat{Z}_k)^T S^{-1} (Z_k - \hat{Z}_k)} \quad (5)$$

where  $S$  is the innovation covariance matrix corresponding to the correct measurement. An ellipsoidal validation region  $\mathcal{V}$  is generated around the target sperm, and only measurements producing a Mahalanobis distance  $d_k$  smaller than the gating threshold are considered valid and used for state update

$$\mathcal{V} = \{Z_k : d_k(Z_k) \leq \gamma\} \quad (6)$$

where  $\gamma$  is the gate threshold corresponding to the gate probability  $P_G$ .

For each valid measurement falling into the validation region  $\mathcal{V}$ , the association probability  $\beta_k(i)$  for the  $i$ -th measurement  $Z_k(i)$  being the correct measurement is calculated according to

$$\beta_k(i) = \frac{\sum_{i=1}^N \mathcal{F}[Z_k(i)]}{1 - P_D P_G \sum_{i=1}^N \mathcal{F}[Z_k(i)]} \quad (7)$$

where

$$\mathcal{F}[Z_k(i)] = |2\pi S|^{-\frac{1}{2}} \exp\left\{-\frac{1}{2} d_k^2[Z_k(i)]\right\}$$

is the likelihood ratio of the measurement  $Z_k(i)$  originating from the target,  $P_D$  is the probability that the target is detected, and  $N$  is the total number of valid measurements. The association probabilities are then used as weights to update state variables

$$X_k = \hat{X}_k + G_k \sum_{i=1}^N \beta_k(i) [Z_k(i) - \hat{Z}_k] \quad (8)$$

where  $G_k$  is the filter gain given in the same way as conventional Kalman filter.

Adding sperm head orientation  $\theta$  effectively helps distinguish the target sperm. Taking Fig. 3(a) as an example, the interfering sperm (black arrow) is in close proximity in terms of  $(x, y)$  position with the target sperm, but the two sperms have different head orientations. The difference in head orientation,  $\theta$  contributes to a larger Mahalanobis distance  $d_k$ . This larger  $d_k$  either makes the measurement of the interfering sperm invalid for state update [see (6)], or leads to a lower association probability of the interfering sperm being the correct measurement [see (7)], thus ensuring that the algorithm correctly tracks the target sperm.

## B. Estimation of Sperm Tail Position

Sperm tail position is estimated based on sperm head position and head orientation. Estimation enables obtaining sperm tail position throughout the immobilization process, even under occlusion by the micropipette during sperm tail tapping

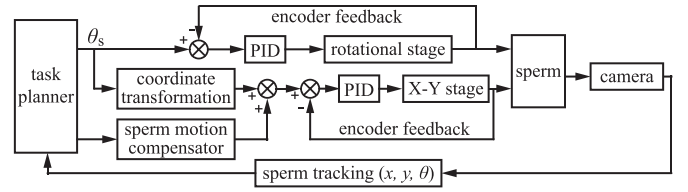


Fig. 4. Control diagram for sperm position and orientation control. The task planner calculates the angle needed for rotational control.

[see Fig. 3(c)]. The estimation approach is made feasible by the fact that the sperm tail is connected to the sperm head by a rigid midpiece. For a healthy sperm, the major axis of the head is aligned with the major axis of the rigid midpiece [30]. Hence, the sperm tail position  $(x_{tail}, y_{tail})^T$  can be accurately estimated by extending the major axis of the sperm head, according to

$$\begin{bmatrix} x_{tail} \\ y_{tail} \end{bmatrix} = \begin{bmatrix} x \\ y \end{bmatrix} - \alpha \begin{bmatrix} \cos \theta \\ \sin \theta \end{bmatrix} \quad (9)$$

where  $\alpha$  is a scalar determining the spatial distance between the estimated tail position and head centroid. Setting a suitable value for  $\alpha$  is critical. If  $\alpha$  is set to be too small, the estimated tail position would be close to the sperm head, and micropipette tapping could damage the sperm head where DNA resides. If  $\alpha$  is set to be too large, the head axis would be extended beyond the actual sperm tail, and micropipette tapping would miss the sperm tail, resulting in immobilization failure.

## IV. SPERM POSITION AND ORIENTATION CONTROL

### A. Task Planning

Visually tracked sperm head information  $(x, y, \theta)$  is used for the control of sperm position and orientation (Fig. 4). Sperm swimming in all directions are categorized into four quadrants based on their head orientation,  $\theta$  [see Fig. 2(d)]. A sperm in the quadrant I or III is ready for micropipette tapping of its tail for immobilization, without the concern of damaging its head. Thus, the system controls the X-Y translational stage to maintain the sperm at the center of the field of view. For a sperm located in the quadrants II or IV, the rotational microscopy stage is also controlled to actively adjust the sperm orientation. Therefore, a task planner is designed to determine the control task for sperms having different orientations (Fig. 4). The output,  $\theta_s$  of the task planner is the angle needed for rotation

$$\theta_s = \begin{cases} 0 & \text{if } \pi/4 \leq |\theta| \leq 3\pi/4 \\ \text{sgn}(\theta) \cdot \pi/2 - \theta & \text{otherwise} \end{cases} \quad (10)$$

where  $\text{sgn}(\theta)$  is the sign function that determines the target orientation of the sperm. The maximum value of  $\theta_s$  is  $\pi/2$ .

### B. 3-DOF Visual Servoing

For 3-DOF visual servo control, the task is to ensure that the target sperm is maintained at the center of field of view and its head orientation is adjusted into the desired quadrant (i.e., quadrant I or III). A potential approach is image-based visual

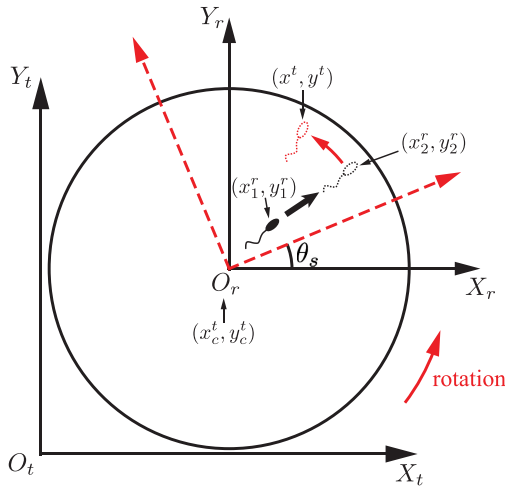


Fig. 5. Coordinate transformation and compensation of sperm movement during movements of the rotational stage and the X-Y translational stage.

servoing. However, a motile sperm does not always align with the rotational center, and the undesired rotation-induced translation can easily move the sperm out of the limited field of view (a few hundreds of micrometers). To keep the target sperm within the field of view, the maximum rotation speed is limited by the distance between the sperm and the rotational axis of the rotational microscopy stage. For instance, at the distance of  $15 \mu\text{m}$  away from the rotational center, the maximum rotation speed is limited to  $42^\circ/\text{s}$  [26]. However, a motile sperm can change its orientation by  $20^\circ$  within 0.3 second ( $67^\circ/\text{s}$ ) [31] due to its wiggly motion, making image-based visual servoing inappropriate to use for sperm orientation control. In contrast, position-based visual servoing does not require keeping the target within the field of view, and thus, the rotational stage could rotate at its maximum angular velocity (i.e.,  $720^\circ/\text{s}$ ), which is sufficiently fast for orientating a motile sperm.

To compensate for rotation-induced translational motion, we choose to use position-based visual servoing and coordinate transformation. As shown in Fig. 5, the coordinate frame of the X-Y translational stage,  $X_t O_t Y_t$  is set as the global coordinate frame. Since the angle needed for rotation  $\theta_s$  is known from the task planner, the target position  $(x_1^t, y_1^t)^T$  of the sperm in the global coordinate frame after rotation can be calculated according to coordinate transformation

$$\begin{bmatrix} x_1^t \\ y_1^t \end{bmatrix} = \begin{bmatrix} \cos \theta_s & -\sin \theta_s \\ \sin \theta_s & \cos \theta_s \end{bmatrix} \begin{bmatrix} x_1^r \\ y_1^r \end{bmatrix} + \begin{bmatrix} x_c^t \\ y_c^t \end{bmatrix} \quad (11)$$

where  $(x_c^t, y_c^t)^T$  is the rotational center in the global coordinate frame and is precalibrated using a commercial calibration slide, and  $(x_1^r, y_1^r)^T$  is the original (before rotation) position of the sperm in the rotational stage coordinate frame  $(X_r O_r Y_r)$ . Since the coordinate axes of the frame  $X_r O_r Y_r$  before rotation are parallel to the coordinate axes of the global coordinate frame  $X_t O_t Y_t$  (Fig. 5),  $(x_1^r, y_1^r)^T = (x_s^t - x_c^t, y_s^t - y_c^t)^T$ , where  $(x_s^t, y_s^t)^T$  is the original sperm position in the global

frame.  $(x_s^t, y_s^t)^T$  can be converted from image feature  $(x, y)^T$  in (1).

Since the sperm continues to move during stage rotation and translation, relying on the result  $(x_1^t, y_1^t)^T$  from coordinate transformation alone cannot make the sperm appear at the center of the field of view after rotation. Due to the presence of multiple sperms surrounding the target sperm, it is difficult to identify the same target sperm before and after rotation. Thus, to reduce the positioning error and ensure the sperm to locate at the center of field of view after rotation, in addition to coordinate transformation, a sperm motion compensator is designed to predict and compensate for the movement of the sperm during stage rotation and translation (Fig. 4).

Prediction of sperm movement is performed in the coordinate frame of the rotational stage  $X_r O_r Y_r$  (Fig. 5). Sperm displacement during stage rotation and translation is determined by both the average speed of the sperm,  $\bar{v}$  and the time cost,  $\Delta t$  for the rotational stage and X-Y translational stage to complete movements. The predicted sperm position,  $(x_2^r, y_2^r)^T$  in the rotational stage frame is

$$\begin{bmatrix} x_2^r \\ y_2^r \end{bmatrix} = \begin{bmatrix} x_1^r \\ y_1^r \end{bmatrix} + \bar{v} \Delta t \begin{bmatrix} \cos \bar{\theta} \\ \sin \bar{\theta} \end{bmatrix} \quad (12)$$

where  $\bar{\theta}$  is the average orientation of the sperm before rotation. Using (12) to replace  $(x_1^r, y_1^r)^T$  with  $(x_2^r, y_2^r)^T$  in (11) gives the compensated target position of the X-Y stage

$$\begin{bmatrix} x^t \\ y^t \end{bmatrix} = \begin{bmatrix} \cos \theta_s & -\sin \theta_s \\ \sin \theta_s & \cos \theta_s \end{bmatrix} \begin{bmatrix} x_1^r + \bar{v} \Delta t \cos \bar{\theta} \\ y_1^r + \bar{v} \Delta t \sin \bar{\theta} \end{bmatrix} + \begin{bmatrix} x_c^t \\ y_c^t \end{bmatrix} \quad (13)$$

In (12),  $\Delta t$  denotes the time taken by the rotational stage and the X-Y translational stage to both complete their movement

$$\Delta t = \max(\theta_s/\omega, \sqrt{(x^t - x_s^t)^2 + (y^t - y_s^t)^2}/v_{stage}) \quad (14)$$

where  $\omega$  is the maximum angular velocity of the rotational stage, and  $v_{stage}$  is the maximum translational velocity of the X-Y stage. Since  $\Delta t$  is determined by  $(x^t, y^t)^T$ , substituting the nonlinear equation (14) into (13) does not result in analytical solutions. Since the speed of a motile sperm (tens of  $\mu\text{m}/\text{s}$ ) is far lower than the translational velocity of the X-Y stage (tens of thousands of  $\mu\text{m}/\text{s}$ ), the time cost for the X-Y stage movement is negligible. Hence, the target position  $(x_1^t, y_1^t)$  of the X-Y translational stage with pure coordinate transformation is used to calculate  $\Delta t$ . Equation (14) becomes

$$\Delta t = \max(\theta_s/\omega, \sqrt{(x_1^t - x_s^t)^2 + (y_1^t - y_s^t)^2}/v_{stage}) \quad (15)$$

After position-based 3-DOF visual servoing,  $\theta_s$  in (10) is set to zero, and the system switches to image-based 2-DOF visual servoing (i.e., X-Y translation) to maintain the target sperm at the center of the field of view for sperm tail tapping.

### C. Sperm Tail Tapping

When the sperm is moved to the center of field of view with a proper orientation, the system controls the micromanipulator to tap the sperm tail with the micropipette for immobilization.

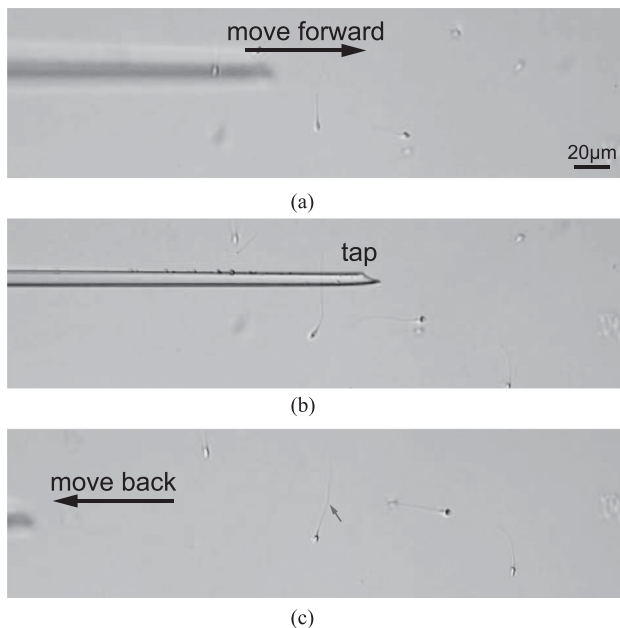


**Fig. 6.** Robotic sperm tail tapping. (a) The system moves micropipette to  $30\ \mu\text{m}$  to the left of the sperm tail position. (b) The micropipette is lowered to tap the sperm tail by pressing it against the substrate surface. (c) A kink (the red arrow) is created on the sperm tail by micropipette tapping. The micropipette is moved back to its resting position.

The micromanipulator first positions the micropipette  $30\ \mu\text{m}$  to the left of the sperm tail position  $(x_{tail}, y_{tail})^T$  [Fig. 6(a)]. Then the micromanipulator moves horizontally to the right by  $60\ \mu\text{m}$  at a speed of  $100\ \mu\text{m/s}$ . This relatively low velocity is intentionally set to avoid generating disturbances in fluid flow that can undesirably displace the sperm. The micropipette is then lowered by  $30\ \mu\text{m}$ , exceeding the original height of the micropipette above the substrate, to press the sperm tail against the substrate [Fig. 6(b)]. This contact and tapping process damages the molecular motors inside the sperm tail and immobilizes the sperm [32] [see the kink created on sperm tail by micropipette tapping in Fig. 6(c), red arrow]. The micropipette is then moved back to its original position in X-Y and  $25\ \mu\text{m}$  above the substrate in Z, and the system is ready for performing the next sperm tail immobilization operation.

## V. EXPERIMENTAL RESULTS AND DISCUSSION

Human sperm samples used in experiments were obtained from CReATe Fertility Centre (Toronto) and informed consent was obtained from all subjects. For all experiments, fresh human sperms were placed on a glass slide containing a droplet of culture medium ( $5\ \mu\text{L}$  PVP solution with HSA, Irvine Scientific) covered by mineral oil to prevent evaporation, as performed in standard clinical practice [33].

### A. Performance of Visual Tracking

**1) Success Rate of Sperm Head Tracking:** To evaluate the effect of interference from other sperms on the success rate of sperm head tracking, 100 sperms were separated into two groups

**TABLE I**  
SUCCESS RATES OF SPERM HEAD TRACKING IN CLINICAL SAMPLES

sample	S1	S2	S3	total
number of sperms	15	17	18	50
success rate of NN	40.0%	47.1%	50.0%	46.0%
success rate of standard PDAF	73.3%	70.6%	72.2%	72.0%
success rate of adapted PDAF	100.0%	94.1%	94.4%	96.0%

(50 sperms per group). Different from clinical samples, sperms in the first group were intentionally diluted (less than  $1 \times 10^7$  cells/ml) such that no interference from surrounding sperms was present. The second group used typical densities of clinical samples ( $2\text{--}5 \times 10^7$  cells/ml), and only those sperms interfered by other sperms were selected for visual tracking. Performance of our adapted PDAF algorithm was compared with that of the standard PDAF algorithm [22] and the nearest neighbor (NN) tracking method [17], [23], [24]. All three algorithms were applied to track the same sperms for 30 continuous image frames. Sperm head tracking was considered successful when the tracked sperm head position was within the sperm head contour throughout the 30 frames of images.

All three algorithms achieved a 100% (50/50) success rate for tracking sperms in the first group that had no interference among sperms. For the second group where the target sperms were interfered by other sperms, the success rate of the commonly used NN method dropped significantly to 46.0% (23 out of 50, see Table I) because the NN method always assumes the nearest measurement to the target to be the correct measurement but does not consider the uncertainty that this nearest measurement may originate from an interfering sperm. Different from the NN method, the standard PDAF method modeled the uncertainty and achieved a higher success rate of 72.0% (36 out of 50). However, the algorithm failed when an interfering sperm was sufficiently close to the target sperm [Fig. 7(a)]. Since only the spatial distance was considered in the standard PDAF algorithm, any sperm sufficiently close to the target sperm, regardless of the interfering sperm's orientation, fell into the validation region,  $\mathcal{V}$  (6), resulting in tracking failures.

The adapted PDAF method used sperm head orientation to effectively distinguish the interfering sperms and achieved a high success rate of 96.0% (48 out of 50). It failed when a highly proximal sperm swam in almost the same orientation as the target sperm [Fig. 7(b)]. In these rare cases, measuring the two sperms both produced a small Mahalanobis distance (5), and the resulting head position was in between the two sperms but not on either of them. Overall, the achieved tracking success rate of 96.0% enables robust sperm tracking under interference in a clinical sample.

**2) Accuracy of Sperm Tail Position Estimation:** The Euclidean distance difference between the algorithm-computed sperm tail position and the human operator-measured sperm tail position was quantified. To obtain benchmark of sperm tail positions, a human operator zoomed in the recorded images and identified the tail positions with best care. Since the estimated tail position is determined by the distance  $\alpha$  to the head centroid

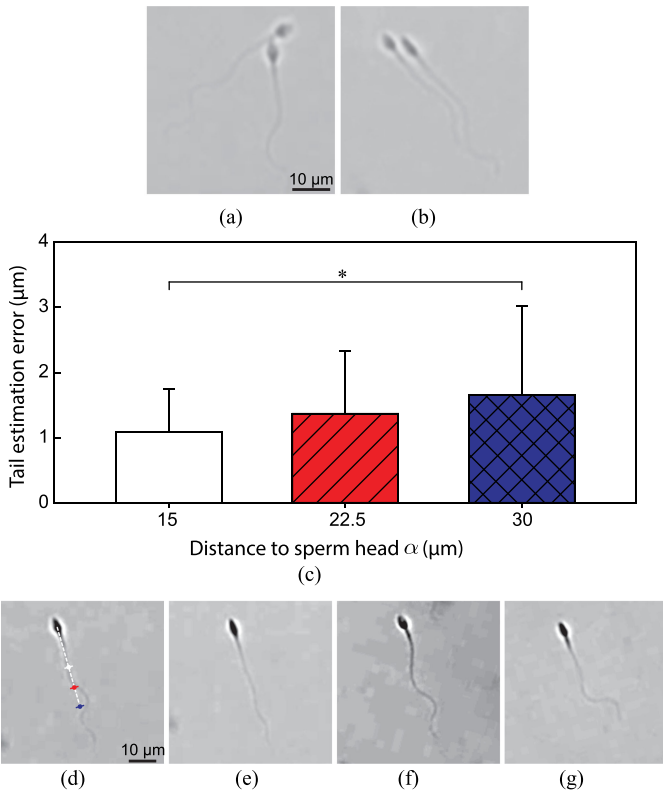


Fig. 7. (a) When two sperms were close in their spatial positions but with different head orientations, our adapted PDAF algorithm succeeded in tracking the target sperm while the standard PDAF algorithm failed. (b) Both the standard PDAF algorithm and our adapted PDAF algorithm failed when an interfering sperm swam in almost the same direction as the target sperm. (c)–(d) Tail estimation error for different values set for  $\alpha$ . \* indicates significant difference ( $p < 0.05$ ). (e)–(g) Sperms have different tail beating amplitudes, resulting in standard deviations (error bars). The contrast of images in (d)–(g) was enhanced off line for better visualization of sperm tails.

in (9), estimation error was evaluated for different values of  $\alpha$  [Fig. 7(c)]. Considering the outer diameter of the micropipette ( $\sim 10 \mu\text{m}$ ), setting a smaller  $\alpha$  has a higher risk of contacting/damaging the sperm head, while setting a larger  $\alpha$  would miss the sperm tail for tapping.

The range of  $\alpha$  was experimentally determined to be between  $15 \mu\text{m}$  and  $30 \mu\text{m}$ . Based on measuring 90 sperms, the results showed that for  $\alpha = 15 \mu\text{m}$ , the average error was  $1.08 \pm 0.66 \mu\text{m}$  (mean  $\pm$  standard deviation), and for  $\alpha = 30 \mu\text{m}$ , the average error was  $1.65 \pm 1.35 \mu\text{m}$ . The errors resulted from the fact that the sperm head position and orientation were used to estimate the sperm tail position, and the curvilinear sperm tail was approximated with a straight line, as described in (9). At a shorter distance to the head centroid, the sperm tail is more straight and better aligned with the extended head axis [see Fig. 7(d)], resulting in smaller estimation errors. The standard deviation in the estimation error originates from variations in the beating behavior of sperm tails. For instance, the sperm shown in Fig. 7(e) beats its tail with a smaller lateral displacement (i.e., beating amplitude) than the sperms shown in Fig. 7(f)(g). In all our subsequent experiments,  $\alpha$  was set to be  $15 \mu\text{m}$  away from the sperm head centroid.

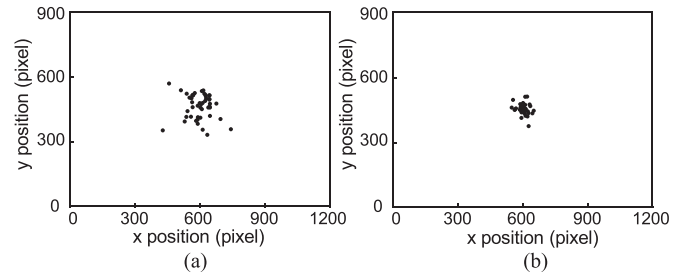


Fig. 8. Sperm positions in the field of view after 3-DOF visual servo control following. (a) Pure coordinate transformation. (b) Prediction and compensation of sperm movement during stage motion. For each group and data plot,  $n = 50$  sperms.

### B. Sperm Orientation Control

To evaluate the performance of the system for predicting and compensating for sperm motions, 100 sperms that were originally in quadrant II and IV were separated into two groups (50 sperms per group). For the first group of sperms, pure coordinate transformation was conducted, and the X-Y translational stage was servoed according to (11). For the second group of sperms, sperm motion was predicted and compensated for and the X-Y translational stage was servoed according to (13). The 100 chosen sperms had random speeds and random distances to the rotational center. In these comparison studies, the outer loop of sperm tracking in Fig. 4 was disabled so that sperm positions immediately after 3-DOF visual servoing were recorded and compared.

After the movement of the rotational stage, all the sperms (100 out of 100 sperms) were successfully brought back into the field of view (Fig. 8), and their orientations were all successfully adjusted into the desired quadrants (i.e., quadrant I or III). Sperm positions in the first group [Fig. 8(a)] were more widely spread out than the second group [Fig. 8(b)], with a significantly higher average positioning error/distance to the center of the field of view ( $25.12 \pm 13.87 \mu\text{m}$  vs.  $5.16 \pm 5.10 \mu\text{m}$ ,  $p < 0.05$ ). The larger positioning error in the pure coordinate transformation group was caused by sperm movement during stage rotation and translation while the sperm movement was not predicted or compensated for as in the second group. Both the rotational and translational stages reached their target positions within 1 second, within which a healthy sperm can produce displacements as large as  $\sim 25 \mu\text{m}$ . The positioning error in the second group is mainly due to the error in predicting sperm movement. The prediction made by (12) was based on the assumption that the sperm moves linearly at a constant speed. In reality a sperm may move along a curvilinear path and/or change its speed, causing prediction errors. Despite of the prediction errors, compensating for sperm movement during stage motion was experimentally proven effective for significantly reducing final positioning errors.

### C. Success Rates of Robotic Immobilization

Robotic sperm immobilization was conducted on 400 sperms to evaluate the overall success rate. Immobilization was considered successful when the correct target sperm (i.e., indicated by

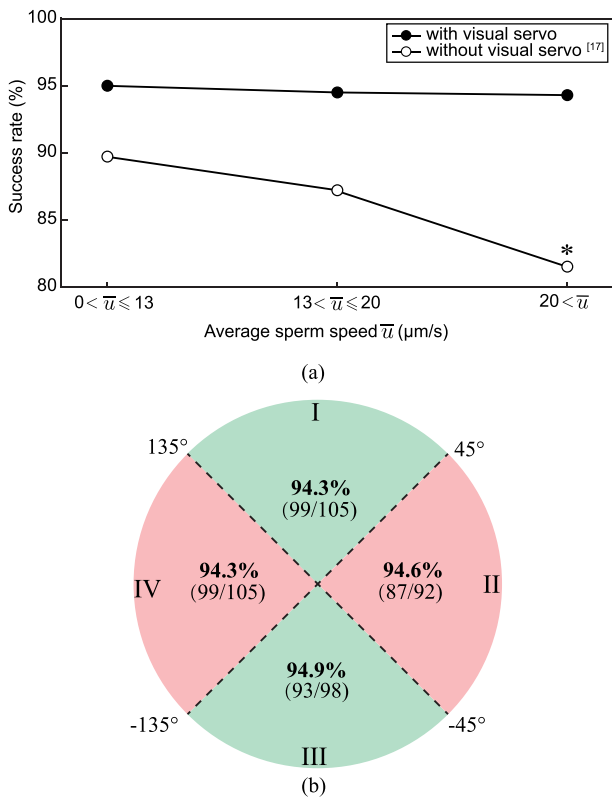


Fig. 9. Sperm immobilization success rate. (a) With visual servo control kept on over the entire duration of sperm immobilization and accurate prediction of sperm movements, consistent success rates were achieved, independent of sperm speeds. (b) The system is capable of immobilizing target sperms swimming in any direction (all quadrants) with consistent success rates.

human operator) was successfully tapped by the micropipette tip and lost its motility. The average time for immobilizing a sperm was 5–6 seconds, including indicating a target sperm, visual tracking, sperm orientation/position adjustment, and micropipette tapping. This time cost could be further improved, for instance, via better optimized motion planning in micropipette tapping. The experimental results showed that 378 out of 400 sperms were successfully immobilized, yielding a success rate of 94.5% in robotic sperm immobilization. Failures occurred when the system lost track of the sperm in visual tracking, such as due to interfering sperms with almost identical orientations as the target sperm [Fig. 7(b)].

For sperms moving at different speeds, we categorized the sperms into three groups [Fig. 9(a)] according to their average speed  $\bar{v}$ . Due to the lack of feedback, previous robotic sperm manipulation [17] lacked the ability of maintaining a target sperm at the center of the field of view or accurately predicting sperm position changes during micropipette movements. The micropipette failed to tap the sperm tail or pressed on the very end of the sperm tail which was insufficient for immobilizing the sperm. As a result, the success rate dropped significantly with increasing sperm speed (from 89.7% to 81.5%). In contrast, this work achieved a consistent success rate of 94.5% with the new robotic system via keeping visual servo control on over the

entire duration of sperm immobilization to always maintain the target sperm at the center of the field of view.

The system also achieved a consistent success rate in all four quadrants [Fig. 9(b)]. In clinical sperm immobilization that is presently manually conducted, the operator waits for the target sperm to change its orientation by itself into quadrant I and III or has to discard it and select another sperm. This limitation is successfully overcome by our robotic system. The robotic system experimentally demonstrated its capability of automated sperm immobilization with a high success rate, regardless of variations in speed or orientation of target sperms.

## VI. CONCLUSION

This paper reported a robotic system for automated immobilization of motile sperms for clinical ICSI. The system integrated an adapted probabilistic data association filter algorithm for sperm head tracking (success rate: 96.0%) under clinical conditions where the target sperm is occluded and interfered by other sperms. Based on the sperm head position, position of the sperm tail was estimated with an accuracy of  $1.08 \mu\text{m}$ . Enabled by a motorized rotational stage and a new position-based visual servo control strategy, the robotic system was capable of actively adjusting sperm orientation and achieved the immobilization of a sperm swimming in any direction. Experiments on 400 sperms with different swimming speeds and directions revealed a consistent success rate of 94.5% for immobilization with an average immobilization time of 5–6 seconds. Robotic sperm immobilization eliminates the skill requirements in manual operation, and is an essential towards automated ICSI. Next steps include further improvement of system throughput and clinical validation.

## REFERENCES

- [1] A. Itoh, "Motion control of protozoa for bio-MEMS," *IEEE/ASME Trans. Mechatronics*, vol. 5, no. 2, pp. 181–188, Jun. 2000.
- [2] V. Magdanz *et al.*, "Spermatozoa as Functional Components of Robotic Microswimmers," *Adv. Mater.*, vol. 29, no. 24, pp. 1–18, 2017.
- [3] P. Vanderzwalmen *et al.*, "Two essential steps for a successful intracytoplasmic sperm injection: Injection of immobilized spermatozoa after rupture of the oolema," *Human Reproduction*, vol. 11, no. 3, pp. 540–7, 1996.
- [4] P. Rubino *et al.*, "The ICSI procedure from past to future: A systematic review of the more controversial aspects," *Human. Reproduction Update*, vol. 22, no. 2, pp. 194–227, 2016.
- [5] G. D. Palermo *et al.*, "Aggressive sperm immobilization prior to intracytoplasmic sperm injection with immature spermatozoa improves fertilization and pregnancy rates," *Human Reproduction*, vol. 11, no. 5, pp. 1023–1029, 1996.
- [6] A. Barroso *et al.*, "Optical assembly of bio-hybrid micro-robots," *Biomed. Microdevices*, vol. 17, no. 2, pp. 1–8, 2015.
- [7] W. Choi *et al.*, "Programmable manipulation of motile cells in optoelectronic tweezers using a grayscale image," *Appl. Phys. Lett.*, vol. 93, 2008, Art. no. 143901.
- [8] D. Nyamjav *et al.*, "Immobilization of motile bacterial cells via dip-pen nanolithography," *Nanotechnology*, vol. 21, no. 23, 2010, Art. no. 235105.
- [9] J. P. Frimat *et al.*, "Make it spin: individual trapping of sperm for analysis and recovery using micro-contact printing," *Lab Chip*, vol. 14, no. 15, pp. 2635–2641, 2014.
- [10] T. Hayakawa *et al.*, "Parallel trapping of single motile cells using vibratin-induced flow on microfluidic chip," in *Proc. IEEE 30th Int. Conf. Micro Electro Mech. Syst.*, 2017, pp. 1281–1284.

- [11] M. Hagiwara *et al.*, "Precise control of magnetically driven microtools for enucleation of oocytes in a microfluidic chip," *Adv. Robot.*, vol. 25, no. 8, pp. 991–1005, 2011.
- [12] M. Dauge *et al.*, "Modelling of a planar magnetic micropusher for biological cell manipulations," *Sens. Actuat. A, Phys.*, vol. 138, no. 1, pp. 239–247, 2007.
- [13] N. Ogawa *et al.*, "Microrobotic visual control of motile cells using high-speed tracking system," *IEEE Trans. Robot.*, vol. 21, no. 4, pp. 704–712, Aug. 2005.
- [14] M. Saito *et al.*, "Ultrasonic manipulation of locomotive microorganisms and evaluation of their activity," *J. Appl. Phys.*, vol. 92, no. 12, pp. 7581–7586, 2002.
- [15] T. G. Cooper and C. H. Yeung, "Computer-aided evaluation of assessment of "grade a" spermatozoa by experienced technicians," *Fertility Sterility*, vol. 85, no. 1, pp. 220–224, 2006.
- [16] E. A. Gaffney *et al.*, "Mammalian sperm motility: Observation and Theory," *Annu. Rev. Fluid Mech.*, vol. 43, no. 1, pp. 501–528, 2011.
- [17] C. Leung *et al.*, "Automated sperm immobilization for ICSI," *IEEE Trans. Biomed. Eng.*, vol. 58, no. 4, pp. 935–942, Aug. 2011.
- [18] J. WilsonLeedy *et al.*, "Development of a novel casa system based on open source software for characterization of zebrafish sperm motility parameters," *Theriogenology*, vol. 67, no. 3, pp. 661–672, 2007.
- [19] R. P. Amann and D. Waberski, "Computer-assisted sperm analysis (casa): Capabilities and potential developments," *Theriogenology*, vol. 81, no. 1, pp. 5–17, 2014.
- [20] S. T. Mortimer *et al.*, "The future of computer-aided sperm analysis," *Asian J. Andrology*, vol. 17, no. 4, p. 545–553, 2015.
- [21] N. A. Swierczek *et al.*, "High-throughput behavioral analysis in *c. elegans*," *Nature Methods*, vol. 8, no. 7, pp. 592–602, 2011.
- [22] L. F. Urbano *et al.*, "Automatic tracking and motility analysis of human sperm in time-lapse images," *IEEE Trans. Med. Imag.*, vol. 36, no. 3, pp. 792–801, Mar. 2017.
- [23] J. Liu *et al.*, "Quantitative analysis of locomotive behavior of human sperm head and tail," *IEEE Trans. Biomed. Eng.*, vol. 60, no. 2, pp. 390–396, Feb. 2013.
- [24] H. F. Yang *et al.*, "Head tracking and flagellum tracing for sperm motility analysis," *2014 IEEE 11th Int. Sympo. Biomed. Imag.*, 2014, pp. 310–313.
- [25] Z. Lu *et al.*, "Robotic icsi (intracytoplasmic sperm injection)," *IEEE Trans. Biomed. Eng.*, vol. 58, no. 7, pp. 2102–2108, Jul. 2011.
- [26] X. Liu *et al.*, "Orientation control of biological cells under inverted microscopy," *IEEE/ASME Trans. Mechatronics*, vol. 16, no. 5, pp. 918–924, Oct. 2011.
- [27] J. Liu *et al.*, "Locating end-effector tips in robotic micromanipulation," *IEEE Trans. Robot.*, vol. 30, no. 1, pp. 125–130, Feb. 2014.
- [28] J. Liu *et al.*, "Automated robotic measurement of 3-D cell morphologies," *IEEE Robot. Autom. Lett.*, vol. 2, no. 2, pp. 499–505, Apr. 2017.
- [29] Y. Bar-Shalom *et al.*, "The probabilistic data association filter," *IEEE Control Syst. Mag.*, vol. 29, no. 6, pp. 82–100, Dec. 2009.
- [30] W. H. Organization, *WHO Laboratory Manual for the Examination and Processing of Human Semen*, 5th ed. Geneva, Switzerland: World Health Organization, 2010.
- [31] Z. Zhang *et al.*, "An automated system for investigating sperm orientation in fluid flow," in *Proc. IEEE Int. Conf. Robot. Autom.*, 2016, pp. 3661–3666.
- [32] K. Yanagida *et al.*, "Influence of sperm immobilization on onset of ca oscillations after ICSI," *Human Reproduction*, vol. 16, no. 1, pp. 148–152, 2001.
- [33] K. Mizuno *et al.*, "Fertilization and embryo development in a mouse ICSI model using human and mouse sperm after immobilization in polyvinylpyrrolidone," *Human Reproduction*, vol. 17, no. 9, pp. 2350–2355, 2002.